optica

Microring resonators on a suspended membrane circuit for atom-light interactions: supplementary material

TZU-HAN CHANG[1], BRIAN M. FIELDS[1], MAY E. KIM[1,†], AND CHEN-LUNG HUNG[1,2,3,*]

[1]Department of Physics and Astronomy, Purdue University, West Lafayette, IN 47907
[2]Purdue Quantum Science and Engineering Institute, Purdue University, West Lafayette, IN 47907
[3]Birck Nanotechnology Center, Purdue University, West Lafayette, IN 47907
[†]Current address: National Institute of Standards and Technology, 325 Broadway, Boulder, CO 80305
[*]Corresponding author: clhung@purdue.edu

Published 11 September 2019

This document provides supplementary information to "Microring resonators on a suspended membrane circuit for atom-light interactions," https://doi.org/10.1364/OPTICA.6.001203.

1. ELECTRIC FIELD PROFILE AND MODE-MIXING IN A MICRORING RESONATOR

A. Mode profile in an ideal microring

Due to the small dimensions of our microring geometry, it supports only fundamental modes within the resonator waveguide at the wavelengths of our interest. A perfect microring supports resonator modes of integer azimuthal mode number m, whose electric field can be written as $\mathbf{E}_{\pm}(\mathbf{r},t) = \mathbf{E}_{\pm}(\mathbf{r})e^{-i\omega t}$, where the spatial field profile in cylindrical coordinates is

$$\mathbf{E}_{\pm}(\mathbf{r}) = \left[\mathcal{E}_{\rho}(\rho,z)\hat{\rho} \pm i\mathcal{E}_{\phi}(\rho,z)\hat{\phi} + \mathcal{E}_{z}(\rho,z)\hat{z}\right] e^{\pm im\phi}. \tag{S1}$$

We additionally require that the mode field satisfies the normalization condition $2\epsilon_0 \int \epsilon(\mathbf{r})|\mathbf{E}_{\pm}(\mathbf{r})|^2 d\mathbf{r} = \hbar\omega$, where ϵ_0 is the vacuum permittivity and $\epsilon(\mathbf{r})$ is the dielectric function. Here, $\mathcal{E}_{\mu}(\rho,z)$ $(\mu = \rho,\phi,z)$ are real functions and are independent of ϕ due to cylindrical symmetry. We note that the azimuthal field component is $\pm\pi/2$ out of phase with respect to the transverse fields due to strong evanescence field decay and transversality of the Maxwell's equation. The perfect resonator modes are traveling waves and the $\pm$ sign indicates the direction of circulation. The mode fields of opposite circulations are complex conjugates of one another $\mathbf{E}_{+}(\mathbf{r}) = \mathbf{E}^{*}_{-}(\mathbf{r})$. We can assign a propagation number $k = m\phi/l$, where $l = R\phi$ is the arc length.

The electric field functions are evaluated using a software employing a finite element method (COMSOL) [1, 2]. Fig. S1 shows the electric field components (in cylindrical coordinates) of the fundamental transverse electric (TE) and transverse magnetic (TM) resonator modes. The fields are slightly asymmetric across the center of the waveguide at $\rho = \rho_w$ due to finite curvature of the microring (radius $R = 16$ μm). We also note that the out-of-phase axial component $i\mathcal{E}_{\phi}$ is stronger in the TM-mode, resulting from stronger evanescent field along the $\hat{z}-$axis where the waveguide confinement is strongly subwavelength.

B. Mode mixing in a microring

In the presence of fabrication imperfections, surface scatters induce radiation loss and mode mixing. The former, together with other intrinsic loss mechanisms (discussed in [3–5]), induces intrinsic resonator energy loss at a rate κ_i. The latter effect can be treated perturbatively, with photons scattered from one resonator mode into another. Assuming small dielectric irregularities in a high-Q resonator, only counter-propagating modes with identical azimuthal number can couple via back-scattering from the surface roughness (at a rate β). In this paper we obtain this back-scattering rate experimentally.

To understand mode-mixing and its impact on the resonator mode profiles, we apply well-established coupled mode theory [6] for two counter propagating modes of interest. Using $a_{-}(a_{+})$ to denote the amplitude of the clock-wise (CW) and counter clock-wise (CCW) propagating resonator modes in a mode-mixed resonator field

$$\mathbf{E}(\mathbf{r},t) = a_{+}(t)\mathbf{E}_{+}(\mathbf{r},t) + a_{-}(t)\mathbf{E}_{-}(\mathbf{r},t), \tag{S2}$$

we have the following coupled rate equation

$$\begin{aligned}\frac{da_{+}}{dt} &= -\left(\frac{\kappa}{2} + i\Delta\omega\right)a_{+}(t) + i\beta e^{i\xi}a_{-}(t)\\ \frac{da_{-}}{dt} &= -\left(\frac{\kappa}{2} + i\Delta\omega\right)a_{-}(t) + i\beta e^{-i\xi}a_{+}(t),\end{aligned} \tag{S3}$$

where $\Delta\omega = \omega - \omega_0$ is the frequency detuning from the bare resonance ω_0, β is the coherent back-scattering rate, and ξ is a

scattering phase shift. The total loss rate $\kappa = \kappa_i + \kappa_c$ includes resonator intrinsic loss rate κ_i and the loss rate κ_c from coupling to the bus waveguide.

Due to the back-scattering terms in Eq. S3 mixing CW and CCW modes, a new set of normal modes are established whose rate equations are decoupled from each other and the frequencies of the new modes are shifted by β and $-\beta$ relative to the unperturbed resonance, respectively. The electric field of the mixed mode can be written as $\mathbf{E}_i(\mathbf{r},t) = \mathbf{E}_i(\mathbf{r})e^{-i\omega t}$ $(i = 1,2)$, where

$$\begin{aligned}\mathbf{E}_1(\mathbf{r}) &= \left[(\mathcal{E}_\rho\hat{\rho} + \mathcal{E}_z\hat{z})\cos(m\phi + \frac{\xi}{2}) - \mathcal{E}_\phi \sin(m\phi + \frac{\xi}{2})\hat{\phi}\right] \\ \mathbf{E}_2(\mathbf{r}) &= i\left[(\mathcal{E}_\rho\hat{\rho} + \mathcal{E}_z\hat{z})\sin(m\phi + \frac{\xi}{2}) + \mathcal{E}_\phi \cos(m\phi + \frac{\xi}{2})\hat{\phi}\right], \quad \text{(S4)}\end{aligned}$$

and we have dropped an overall factor $\sqrt{2}e^{-i\frac{\xi}{2}}$ for convenience. The fields in Eq. S4 should also satisfy the normalization condition. With the presence of back-scattering, the resonator mode polarization now becomes linear but is rotating primarily in the ρ-ϕ (z-ϕ) plane for TE (TM) mode along the microring.

C. Atom-photon coupling in a microring resonator

We consider the atom-photon coupling strength

$$g_i = d_i\sqrt{\frac{\omega}{2\hbar\epsilon_0 V_m}} \quad \text{(S5)}$$

where $d_i = \langle e|\mathbf{d}|g\rangle \cdot \mathbf{u}_i$ is the transition dipole moment, $\mathbf{u}_i = \mathbf{E}_i(\rho_a, z_a)/|\mathcal{E}(\mathbf{r}_a)|^2$ is the electric field polarization vector, $|\mathcal{E}|^2 = |\mathcal{E}_\rho|^2 + |\mathcal{E}_\phi|^2 + |\mathcal{E}_z|^2$, $\hbar$ is the Planck constant divided by 2π, and $V_m(\mathbf{r}_a)$ is the effective mode volume at atomic position $\mathbf{r}_a$,

$$\begin{aligned}V_m(\rho_a, z_a) &= \frac{\int \epsilon(\rho,z)|\mathcal{E}(\rho,z)|^2\rho d\rho dz d\phi}{\epsilon(\rho_a,z_a)|\mathcal{E}(\rho_a,z_a)|^2} \\ &= A_m(\rho_a,z_a)L. \quad \text{(S6)}\end{aligned}$$

Here A_m follows the definition Eq. 1 in the main text and $L = 2\pi R$ is the circumference of the microring.

We note that the coupled modes in Eq. S5 can be the CW and CCW modes, that is $i = \pm$, when $g_i \gg \beta$. On the other hand, if $\beta \gg g_i$, an atom should be coupled to a mixed mode with $i = 1,2$. Our microring platform corresponds to the latter case. We also note that the exact value of the transition dipole moment d_i depends on the atomic location and dipole orientation. In the main text, we simply replace d_i with the reduced dipole moment d, where $d^2 = \frac{3\lambda^3\epsilon_0\hbar\gamma}{8\pi^2}$, and arrive at

$$g = \sqrt{\frac{3\lambda^3\omega\gamma}{16\pi^2 V_m}}. \quad \text{(S7)}$$

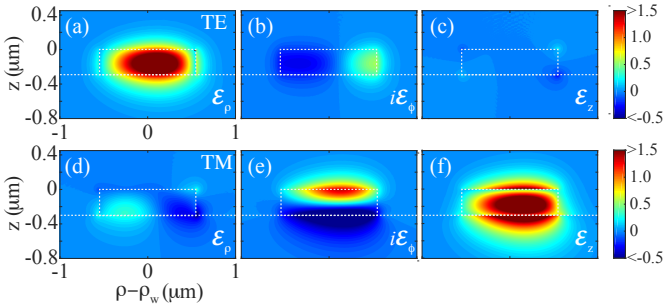

Fig. S1. Electric field vector components $(\mathcal{E}_\rho, i\mathcal{E}_\phi, \mathcal{E}_z)$ of (a-c) the fundamental transverse electric (TE) mode and (d-f) the transverse magnetic (TM) mode (in arbitrary units). Dashed lines mark the boundaries of the dielectrics. Radius of the ring $R = \rho_w = 16$ μm.

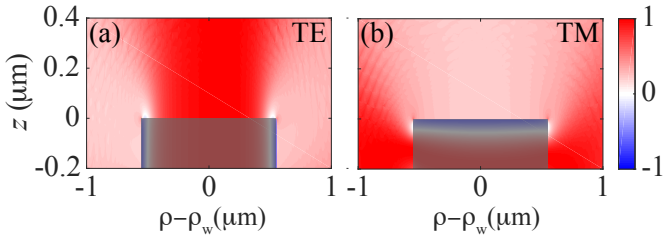

Fig. S2. The visibility amplitude factor $v(\rho,z)$ in the intensity profiles $\mathbf{E}_{1(2)}$ of the mixed TE (a) and TM (b) resonator modes, respectively. Shaded areas mark the microring waveguide.

D. Exciting the resonator mode via an external waveguide

If we consider exciting the resonator mode with input power $|s_\pm|^2$ (actual power P_w normalized with respect to $\hbar\omega$) from either end of the bus waveguide, additional amplitude growth rate $Ks_\pm$ can be added to the right hand side of Eq. S3; in the case of a lossless coupler $K = i\sqrt{\kappa_c}$. Due to phase matching conditions between the linear waveguide and the microring, $s_+(s_-)$ only couples to the CCW(CW) mode and not to the other mode of opposite circulation. In the original CCW/CW basis, the mode amplitudes are

$$\begin{aligned}a_+ &= K\frac{\alpha s_+ + i\beta s_-}{\alpha^2+\beta^2} \\ a_- &= K\frac{i\beta^* s_+ + \alpha s_-}{\alpha^2+\beta^2}, \quad \text{(S8)}\end{aligned}$$

where $\alpha = \frac{\kappa}{2} + i\Delta\omega$. If we now consider exciting the resonator modes from one side of the bus waveguide, the intra-resonator field is

$$\mathbf{E}^\pm(\mathbf{r}) = \frac{\alpha K s_\pm}{\alpha^2+\beta^2}\left[\mathbf{E}_\pm(\mathbf{r}) + \frac{i\beta e^{\mp i\xi}}{\alpha}\mathbf{E}_\mp(\mathbf{r})\right], \quad \text{(S9)}$$

The $\pm$ sign in Eq. (S9) indicates either $|s_+| > 0$ (and $s_- = 0$) or $|s_-| > 0$ (and $s_+ = 0$). With back-scattering mixing counter-propagating modes, the field intensity is a standing wave

$$|\mathbf{E}^\pm(\mathbf{r})|^2 = \mathcal{I}|\mathcal{E}(\rho,z)|^2\left[1 \pm V(\rho,z)\sin(2m\phi + \xi_\pm)\right], \quad \text{(S10)}$$

where $\xi_\pm = \xi \pm \arg(\alpha)$. The sign flip in the intensity corrugation is due to the opposite mixtures of the resonator modes being excited, Eq. (S9), and an overall $\pi/2$ phase shift in the back-scattered mode. We have a frequency-dependent energy build-up factor

$$\mathcal{I} = \mathcal{I}_0\frac{|\alpha|^2+\beta^2}{|\alpha^2+\beta^2|^2}, \quad \text{(S11)}$$

where $\mathcal{I}_0 = \frac{\kappa_c P_w}{\hbar\omega}$ for a lossless coupler and

$$V(\rho,z) = \frac{2|\alpha|\beta}{|\alpha|^2+\beta^2}v(\rho,z) \quad \text{(S12)}$$

is the visibility of the standing wave; $V \le v$ and equality holds when $|\alpha| = \beta$. Here, $v = 1 - 2|\mathcal{E}_\phi|^2/|\mathcal{E}|^2$ is a visibility amplitude

factor. The presence of the axial field reduces the visibility of the standing wave: v vanishes when $|\mathcal{E}_\phi|^2 = |\mathcal{E}|^2/2$ and is largest with $|\mathcal{E}_\phi|^2 = 0$. As shown in Fig. S2, the visibility of the TE mode is $v \approx 1$ above the microring due to the smallness of the axial component. On the contrary, for TM-mode a smaller $v \approx 0.2$ above the waveguide results from large $|\mathcal{E}_\phi|^2$ as seen in Fig. S1.

From Eqs. (S10-S12), we can develop schemes to maximize or minimize standing-wave visibility for evanescent field trapping. This is discussed in the main text and in the following sections.

2. AC STARK SHIFT IN AN EVANESCENT FIELD TRAP

A. Scalar and vector light shifts in the ground state

When a ground state atom is placed above a microring with a strong evanescent field that is far-off resonant from the atomic resonances, it experiences a spatially varying AC stark shift

$$U(\mathbf{r}) = -\alpha_{\mu\nu}(\omega) E_\mu(\mathbf{r}) E_\nu^*(\mathbf{r}), \tag{S13}$$

where $\alpha_{\mu\nu}$ is the dynamic polarizability tensor and $E_\mu = \mathbf{E}\cdot\hat{\mathbf{e}}_\mu$ is the vector components of the microring evanescent field. In the irreducible tensor representation, the above tensor product can be separated into contributions from scalar (rank-0), vector (rank-1), and tensor (rank-2) terms

$$U(\mathbf{r}) = U^s(\mathbf{r}) + U^v(\mathbf{r}) + U^t(\mathbf{r}), \tag{S14}$$

where

$$U^s(\mathbf{r}) = -\alpha^{(0)}(\omega)|\mathbf{E}(\mathbf{r})|^2 \tag{S15}$$

$$U^v(\mathbf{r}) = -i\alpha^{(1)}(\omega)\frac{\mathbf{E}(\mathbf{r})\times\mathbf{E}^*(\mathbf{r})\cdot\hat{\mathbf{F}}}{2F} \tag{S16}$$

$$U^t(\mathbf{r}) = -\alpha^{(2)}(\omega)\frac{3}{F(2F-1)}\times \left[\frac{\hat{F}_\mu\hat{F}_\nu + \hat{F}_\nu\hat{F}_\mu}{2} - \frac{\hat{\mathbf{F}}^2}{3}\delta_{\mu\nu}\right] E_\mu E_\nu^*, \tag{S17}$$

and $\alpha^{(0,1,2)}(\omega)$ are the corresponding scalar, vector, and tensor polarizabilities, $\hat{\mathbf{F}}$ is the total angular momentum operator, and F is the quantum number. We note that, for ground state atoms in the S angular momentum state, $\alpha^{(2)} = 0$. Therefore we do not consider U^t throughout the discussions. The calculations of $\alpha^{(0,1)}$ follow those of [7], using transition data summarized in [8], and is not repeated here. Table S1 lists the value of polarizabilities used in the trap calculation.

λ	$\alpha^{(0)}$ (a.u.)	$\alpha^{(1)}$ (a.u.)	$\alpha^{(1)}/\alpha^{(0)}$
λ_r	3032.67	25.503	0.0084
λ_b	-2110.81	10.047	-0.0048

Table S1. Cesium $6S_{1/2}, F = 4$ ground state dynamic polarizabilities at $\lambda_r = 935.261$ nm and $\lambda_b = 793.515$ nm.

B. Scalar and vector light shifts in an evanescent field trap

To form an evanescent field trap, the microring must be excited through an external waveguide. Equations (S9-S10) can be used to calculate the single-end excited resonator electric field. The complex polarization of a mixed resonator mode induces

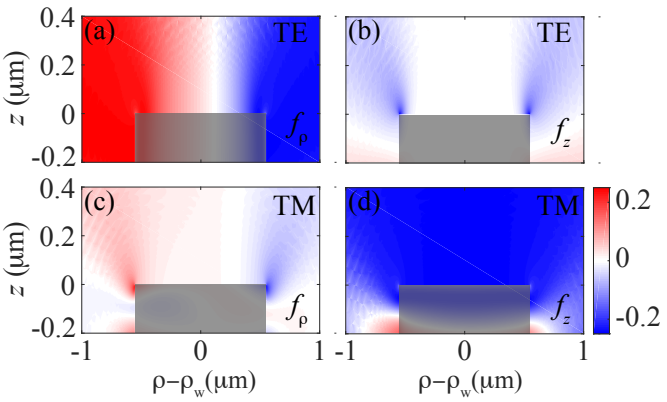

Fig. S3. Vector light shift polarization factor $f_\mu(\rho,z)$ for single-end excited (a-b) TE and (c-d) TM modes, respectively. Shaded areas mark the microring waveguide.

both scalar and vector components of the AC Stark shift. Using $\mathbf{E}(\mathbf{r}) = \mathbf{E}^{\pm}(\mathbf{r})$ from Eq. (S10), the scalar light shift forms a standing-wave potential

$$U^s(\mathbf{r}) = -\alpha^{(0)}(\omega)\mathcal{I}|\mathcal{E}(\rho,z)|^2\left[1 \pm V(\rho,z)\sin(2m\phi + \xi_\pm)\right]. \tag{S18}$$

Meanwhile, the vector light shift depends on the cross product between the CW and CCW components in the excited field

$$\mathbf{E}^{\pm}(\mathbf{r})\times\mathbf{E}^{\pm}(\mathbf{r})^* = \mp 2i\tilde{\mathcal{I}}\mathcal{E}_\phi(\rho,z)\left[\mathcal{E}_\rho(\rho,z)\hat{z} - \mathcal{E}_z(\rho,z)\hat{\rho}\right], \tag{S19}$$

which is smooth along the microring (independent of ϕ coordinate) and varies only in the transverse coordinates (ρ,z). Here, $\tilde{\mathcal{I}}$ is the build up factor for the vector potential

$$\tilde{\mathcal{I}} = \mathcal{I}_0\frac{|\alpha|^2 - \beta^2}{|\alpha^2 + \beta^2|^2}. \tag{S20}$$

In a special case when the atomic principal axis lies along the $\hat{z}$-axis, the vector light shift can be explicitly written as

$$U^v = \mp\alpha^{(1)}(\omega)\tilde{\mathcal{I}}\mathcal{E}_\phi(\rho,z)\times \left[\mathcal{E}_\rho(\rho,z)\frac{\hat{F}_z}{F} - \mathcal{E}_z(\rho,z)\frac{(\hat{F}_+ + \hat{F}_-)}{2F}\right], \tag{S21}$$

where $\hat{F}_\pm$ are the angular momentum ladder operators.

The explicit dependence on angular momentum operators in U^v reveals a diagonal, state-dependent energy shift and off-diagonal coupling terms. Near the anti-nodes of a standing wave Eq. (S10), which should serve as trap centers, the ratio between the vector and the scalar light shifts is found to be (dropping $\hat{\mathbf{F}}$-related factors)

$$\left|\frac{U^v_\mu}{U^s}\right| \sim \frac{\alpha^{(1)}(\omega)}{\alpha^{(0)}(\omega)} \times \frac{\mathcal{E}_\phi(\rho,z)\mathcal{E}_\mu(\rho,z)}{2|\mathcal{E}(\rho,z)|^2}\frac{\tilde{\mathcal{I}}}{\mathcal{I}}, \tag{S22}$$

where U^v_μ $(\mu = \rho, z)$ represent the amplitudes of the diagonal and off-diagonal terms in the vector light shift Eq. (S21), respectively.

Equation (S22) suggests that the state dependent vector light shift can be several orders of magnitude smaller than the scalar shifts. For far-off-resonant light with frequency ω that is largely

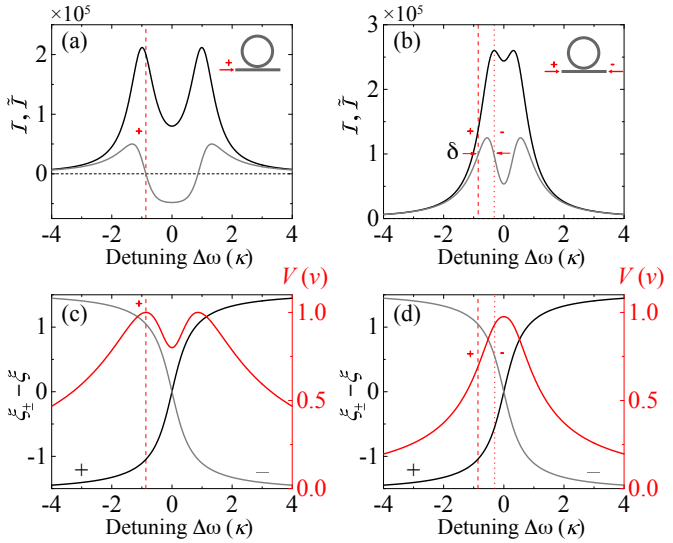

Fig. S4. Coupling schemes to eliminate the vector light shifts for microrings with $\beta > \kappa/2$ (a,c) and $\beta < \kappa/2$ (b,d). (a,b) Intensity build-up factors $\mathcal{I}$ (black curve) and $\tilde{\mathcal{I}}$ (gray curve) for scalar and vector light shifts, respectively, for $\kappa/2\pi = 1$ GHz, and $\beta/2\pi$ = (a)1 GHz and (b)0.4 GHz; $\mathcal{I}_0 = 10^5\kappa^2$. Vertical dash (+) and dotted (-) lines in red indicate the frequency detuning of excited modes for zeroing the vector shifts. $\pm$ signs denote the direction of excitation and the insets illustrate the corresponding coupling schemes. (c,d) Visibility V (red curve) and phase shifts $\zeta_\pm - \zeta$ (black and gray curves) in the standing wave scalar potential Eq. (S18) under the same parameters and coupling schemes as in (a,b), respectively.

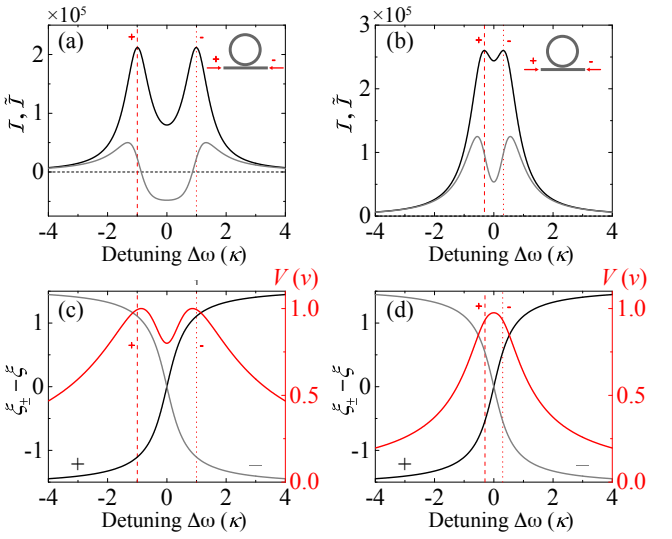

Fig. S5. Coupling schemes to eliminate both the vector light shifts and the standing wave pattern in the scalar potential. Same curves and parameters as those in Fig. S4 are plotted, but with different coupling schemes (insets) and frequencies marked by the vertical dash (+) and dotted (-) lines.

red- or blue-detuned from both cesium D1 and D2 lines, the vector polarizability $\alpha^{(1)}(\omega) \ll \alpha^{(0)}(\omega)$; see Table S1. The electric field polarization factor

$$f_\mu(\rho,z) = \frac{\mathcal{E}_\phi(\rho,z)\mathcal{E}_\mu(\rho,z)}{2|\mathcal{E}(\rho,z)|^2} \tag{S23}$$

provides additional suppression. As shown in Fig. S3, a TE mode supports an off-diagonal factor $f_\rho \approx 0$ and the diagonal factor $f_z \approx 0.07$. For a TM mode, $f_\rho \approx -0.24$ and $f_z \approx 0.01$. We expect a single-end coupled evanescent wave potential leads to $|\frac{U^v}{U^s}| \lesssim 10^{-3}$.

C. Eliminating the vector light shifts

In practical experiments, a state-independent trap is much preferred since it prevents parasitic effects such as dephasing or trap heating. To fully eliminate the vector shift, a straightforward method is to choose a proper detuning such that $\beta = |\alpha|$ (provided that $\beta > \kappa/2$) and $\tilde{\mathcal{I}} = 0$, as suggested by Eqs. (S20-S21) and illustrated in Fig. S4 (a). Visibility V is at the same time maximized as $|\alpha| = \beta$ creates equal superposition of CW and CCW modes up to a relative phase shift, as seen in Eq. S9. The excited field becomes linearly polarized with spatially rotating polarization, similar to the form in Eq. S4, and leads to zero vector shift. In this simple scheme, the scalar light shift build-up factor is also near its maximal value, as in Fig. S4(a, c).

In cases when $\beta < \kappa/2$, a second option is to excite the resonator from both ends of the external waveguide, with one frequency aligned to the resonance peak $\mathcal{I}_- = \mathrm{Max}(\mathcal{I})$ and another one aligned such that the two excited fields have equal build-up factors $\tilde{\mathcal{I}}_+ = \tilde{\mathcal{I}}_-$ as shown in Fig. S4 (b). Due to large relative frequency detuning δ between the two fields, their contributions to the vector light shift, Eq. (S21), are of opposite signs and can be summed up incoherently to completely cancel each other. The standing wave pattern in the total scalar shift [Eq. (S18)], on the other hand, still remains highly visible. For the example shown in Fig. S4 (b, d), the two excited fields have unequal intensity buil-up factors, $(\mathcal{I}_+, \mathcal{I}_-) \approx (2.6, 1.4) \times 10^3$, visibilities $(V_+, V_-) \approx (0.93v, 0.69v)$ and a differential standing-wave phase shift $|\xi_+ - \xi_-| \approx 0.49\pi$. The incoherent sum of the scalar light shifts results in a new visibility

$$V' = \frac{\sqrt{(\mathcal{I}_+V_+)^2 + (\mathcal{I}_-V_-)^2 - 2\mathcal{I}_+\mathcal{I}_-V_+V_-\cos|\xi_+ - \xi_-|}}{(\mathcal{I}_+ + \mathcal{I}_-)}, \tag{S24}$$

which gives $V' \approx 0.65v$ and the standing wave pattern remains sufficiently strong.

D. Eliminating standing wave in the scalar potential

Modifications in the previous schemes allow further elimination of the standing wave potential. We make use of the fact that the standing wave patterns can be created 180 degrees out of phase with respect to each other when we excite the microring from either end of the bus waveguide with exact opposite frequency detuning to the bare resonance ω_0, as shown in Fig. S5 for $\beta > \kappa/2$ (a,c) and $\beta < \kappa/2$ (b,d). Since we also have equal energy build-up factors and visibilities, $(\mathcal{I}, \tilde{\mathcal{I}}, V)$, the standing wave pattern as well as the vector light shift can be fully cancelled, allowing us to create a state-independent, smooth evanescent field potential along the microring that is highly useful in our two-color trapping scheme.

3. LOSSES IN MICRORING RESONATORS

A. Fundamental limits of the microring platform

Without considering fabrication imperfections, the cooperativity parameter is fundamentally limited by the intrinsic quality factor

$Q_i \sim 1/(Q_a^{-1} + Q_b^{-1})$ due to finite material absorption (Q_a) and the bending loss (Q_b). For stoichiometric LPCVD nitride films, it has been estimated that the absorption coefficient $\alpha \ll 1$ dB/m in the near infrared range [4]. At cesium D1 and D2 wavelengths, for example, we estimate that $Q_a \gtrsim 10^8$ should contribute little to the optical loss in a fabricated microring. On the other hand, we numerically estimate the bending loss from FEM analysis. We have empirically found that $Q_b \gg 10^8$ when the radius of a microring is beyond 15 micron, as in our case, and the effective refractive index of the resonator mode is $n_{\text{eff}} > 1.65$, constraining the minimum mode volume to be $V_m \gtrsim 500\lambda^3$ for an atom trapped around $z_t \gtrsim 75$ nm ($V_m \gtrsim 50\lambda^3$ for a solid state emitter at the waveguide surface). Without further considering fabrication imperfections, the fundamental limit for the cooperativity parameter could be as high as $C \sim 10^{-4} Q_a \gtrsim 10^4$ ($\gtrsim 10^5$ on the waveguide surface).

B. Surface scattering loss

The analysis of surface scattering loss has been greatly discussed in the literature, see [3, 9, 10] for example. Here we adopt an analysis similar to [3], but with a number of modifications. We evaluate the surface scattering limited quality factor by calculating

$$Q_{ss} = \frac{\omega U_c}{P_{ss}}, \tag{S25}$$

where $U_c = \frac{1}{2}\epsilon_0 \int \epsilon(\mathbf{r})|\mathbf{E}(\mathbf{r})|^2 d^3r$ is the energy stored in the ring, $\epsilon(\mathbf{r})$ and $\mathbf{E}(\mathbf{r})$ are the unperturbed dielectric function and the resonator mode field, respectively, and P_{ss} is the radiated power due to surface scattering.

We adopt the volume current method [11] to calculate the radiation loss. To leading order, the radiation vector potential is generated by a polarization current density $\mathbf{J} = -i\omega\delta\epsilon\mathbf{E}$ created by the dielectric defects, where $\delta\epsilon(\mathbf{r})$ is the dielectric perturbation function that is non-zero only near the four surfaces of the microring. In the far field, we have

$$\mathbf{A} = \frac{\mu_0}{4\pi}\frac{e^{-i\mathbf{k}\cdot\mathbf{r}}}{r}\int \left[-i\omega\delta\epsilon(\mathbf{r}')\mathbf{E}(\mathbf{r}')\right] e^{-i\mathbf{k}\cdot\mathbf{r}'} d^3r'. \tag{S26}$$

The radiation loss can thus be estimated by the time averaged Poynting vector.

We note that the above method works best for a waveguide embedded in a uniform medium [11]. In our case, a nitride waveguide on a dioxide substrate embedded in vacuum, an accurate calculation is considerably more complicated due to dielectric discontinuities in the surrounding medium. Here, we neglect multiple reflections and estimate the amount of scattering radiation in the far field (in vacuum) by separately evaluating the contributions from the four surfaces of a microring waveguide. We take $\delta\epsilon_i = \epsilon_0(\epsilon - \epsilon_i)\Delta_i(\mathbf{r})$, where ϵ and ϵ_i are the dielectric constants of nitride and the surrounding dioxide substrate or vacuum, respectively, and $\Delta_i(\mathbf{r})$ represents the distribution function of random irregularities near the i-th surface. For the side walls at $\rho_\pm = R \pm W/2$, surface roughness caused by etching imperfections; for top and bottom surfaces at $z = z_{t,b}$, this results from imperfect film growth.

Using, Eqs. (S26), we could then evaluate

$$\begin{aligned} P_{ss} &= \int \frac{\omega k}{2\mu_0}|\mathbf{r}\times\mathbf{A}|^2 d\Omega \\ &= \frac{\omega k^3 \epsilon_0}{32\pi^2}\sum_{i,\alpha}(\epsilon-\epsilon_i)^2 C_{i,\alpha}, \end{aligned} \tag{S27}$$

where

$$\begin{aligned} C_{i,\alpha} = \int d\Omega \int\int \mathcal{E}_\alpha(\mathbf{r}')\mathcal{E}^*_\alpha(\mathbf{r}'') e^{-i\mathbf{k}\cdot(\mathbf{r}'-\mathbf{r}'')+im(\phi'-\phi'')} \\ \times (\hat{\mathbf{r}}\times\hat{\mathbf{e}}'_\alpha)\cdot(\hat{\mathbf{r}}\times\hat{\mathbf{e}}''_\alpha)\Delta_i(\mathbf{r}')\Delta_i(\mathbf{r}'') d^3r' d^3r''. \end{aligned} \tag{S28}$$

The random roughness in the second line of the integral varies at very small length scale $\ll \lambda$, as suggested by our AFM measurements. Thus, the electric field related terms in the first and the second lines above can be considered slow-varying. The integration over large ring surfaces should sample many local patches of irregularities, each weighed by similar electric field value and polarization orientation. We may thus replace $\Delta_i(\mathbf{r}')\Delta_i(\mathbf{r}'')$ with an ensemble averaged two-point correlation function $\langle\Delta_i(\mathbf{r}')\Delta_i(\mathbf{r}'')\rangle$, which can be determined from the AFM measurements. We approximate the two-point correlation with a Gaussian form

$$\begin{aligned} &\langle\Delta_i(\mathbf{r}')\Delta_i(\mathbf{r}'')\rangle \approx \\ &\quad \sigma_i^2 e^{-\frac{(\mathbf{r}'-\mathbf{r}'')^2}{L_i^2}}\delta(z'-z_i)\delta(z''-z_i)\Theta(\rho')\Theta(\rho'') \end{aligned} \tag{S29}$$

for top and bottom surfaces ($i = t, b$) and, similarly,

$$\begin{aligned} &\langle\Delta_i(\mathbf{r}')\Delta_i(\mathbf{r}'')\rangle \approx \\ &\quad \sigma_i^2 e^{-\frac{R_i^2(\phi'-\phi'')^2}{L_i^2}}\delta(\rho'-\rho_i)\delta(\rho''-\rho_i)\Theta(z')\Theta(z'') \end{aligned} \tag{S30}$$

for the side walls ($i = \pm$). In the above, σ_i and L_i are the root-mean-squared roughness and the correlation length, respectively. $\delta(x)$ is the Dirac delta function, and $\Theta(x) = 1$ for x lying within the range of the (perfect) ring waveguide and $\Theta(x) = 0$ otherwise.

Plugging Eq. (S29) into Eq. (S28) to evaluate loss contribution from top and bottom roughness, we obtain

$$C_{i,\alpha} \approx \sigma_i^2 \int\int d\rho' d\rho'' \rho'^2 |\mathcal{E}_\alpha(\rho', z_i)|^2 e^{-\frac{(\rho'-\rho'')^2}{L_i^2}}\Phi_\alpha(\rho'), \tag{S31}$$

where, due to the short correlation length $L_i \ll \lambda$, we can simplify the azymuthal part of the integral by taking $\rho'' \approx \rho'$ and arrive at the following

$$\begin{aligned} \Phi_\alpha &= \int d\Omega \int d\phi' d\phi'' (\hat{\mathbf{r}}\times\hat{\mathbf{e}}'_\alpha)\cdot(\hat{\mathbf{r}}\times\hat{\mathbf{e}}''_\alpha)\times \\ &\quad e^{im(\phi'-\phi'')} e^{-ik\frac{\rho}{r}\rho'(\cos\phi'-\cos\phi'')} e^{-\frac{\rho'^2(\phi'-\phi'')^2}{L_i^2}} \\ &\sim 4\pi^{5/2}\eta\frac{L_i}{\rho'}. \end{aligned} \tag{S32}$$

In the above, we used the fact that the integrant is none-vanishing only when $|\phi'-\phi''| \lesssim L_i/R \ll 1$ and $m|\phi'-\phi''| \sim kL_i \lesssim 1$. Here $\eta = \frac{4}{3}$ is a geometric radiation parameter due to mode-field polarizations coupled to that of freespace radiation modes [3]; We note that η is polarization independent, different from the result of [3], because the surface scatterers are approximately spherically symmetric ($\sigma_i, L_i \ll \lambda$) in the sense of radiation at farfield.

Plugging Eq. (S32) into Eq. (S31), we arrive at

$$\begin{aligned} C_{t(b),\alpha} &\approx 4\pi^{5/2}\sigma^2_{t(b)} L^2_{t(b)} RW\eta |\bar{\mathcal{E}}_{t(b),\alpha}|^2 \\ &= \frac{16}{3}\pi^{5/2} V^2_{t(b)} |\bar{\mathcal{E}}_{t(b),\alpha}|^2, \end{aligned} \tag{S33}$$

where $|\bar{\mathcal{E}}_{\mathrm{t(b)},\alpha}|^2 = \frac{1}{RW}\int_{\rho_-}^{\rho_+}\rho'|\mathcal{E}_\alpha(\rho', z_{\mathrm{t(b)}})|^2 d\rho'$ is the averaged mode field and $V_{\mathrm{t(b)}} \equiv \sigma_{\mathrm{t(b)}} L_{\mathrm{t(b)}}\sqrt{RW}$ is the effective volume of the scatterers.

For scattering contributions due to side wall roughness, we adopt similar procedures and obtain

$$C_{\pm,\alpha} \approx \frac{16}{3}\pi^{5/2} V_\pm^2 |\bar{\mathcal{E}}_{\pm,\alpha}|^2, \tag{S34}$$

where the effective volume is $V_\pm = \sigma_\pm H\sqrt{L_\pm \rho_\pm}$, the effective mode field $|\bar{\mathcal{E}}_{\pm,\alpha}|^2 = \frac{1}{\eta H^2}\int_{-1}^{1}|\tilde{\mathcal{E}}_{\pm,\alpha}(\tilde{k})|^2\eta_\alpha(\tilde{k})d\tilde{k}$ and $\tilde{\mathcal{E}}_{\pm,\alpha}(\tilde{k}) = \int_0^H \mathcal{E}_\alpha(\rho_\pm, z')e^{-ik\tilde{k}z'}dz'$. Here, η_α is polarization dependent due to the geometric shape of the side wall roughness, with $\eta_{\rho(\phi)}(\tilde{k}) = \frac{1}{2}(1+\tilde{k}^2)$ and $\eta_z = 1-\tilde{k}^2$.

We note that the apparent difference between the mode field contributions in Eqs. (S33) and (S34) is due to the effective volume of the surface and side wall scatterers. At the side walls, because the vertical length of the edge roughness is about the thickness H of the waveguide and is rather comparable to the wavelength, interference effect manifests and modifies the scattering contribution from the mode field $|\bar{\mathcal{E}}_{\pm,\alpha}|^2$. If $kH \ll 1$, $|\bar{\mathcal{E}}_{\pm,\alpha}|^2 \approx |\int_0^H \mathcal{E}_\alpha(R_\pm, z')dz'/H|^2$ gives the averaged mode field squared at the side walls.

We then evaluate the scattering-loss quality factor as

$$Q_{\mathrm{ss}} = \frac{32\pi^2 U_{\mathrm{c}}}{k^3\epsilon_0\sum_{i,\alpha}\Delta\epsilon_i^2 C_{i,\alpha}} \tag{S35}$$

$$= \frac{3\lambda^3}{8\pi^{7/2}\sum_{i,\alpha}\Delta\epsilon_i^2 V_i^2|\bar{u}_{i,\alpha}|^2}, \tag{S36}$$

where $\Delta\epsilon_i = \epsilon - \epsilon_i$ and define

$$|\bar{u}_{i,\alpha}|^2 \equiv \frac{|\bar{\mathcal{E}}_{i,\alpha}|^2}{\int\epsilon(\mathbf{r})|\mathbf{E}(\mathbf{r})|^2 d^3r} \tag{S37}$$

$$\approx \frac{|\bar{\mathcal{E}}_{i,\alpha}|^2}{2\pi R\int\epsilon(\mathbf{r})\sum_\alpha|\mathcal{E}_\alpha(\rho,z)|^2 d\rho dz} \tag{S38}$$

as the normalized, weighted mode field energy density.

In the main text we optimize Q/V_{m} by calculating $Q = 1/(Q_{\mathrm{b}}^{-1} + Q_{\mathrm{ss}}^{-1})$. From Eq. (S36) with given roughness parameters, it is clear that Q_{ss} can be made higher by increasing the degree of mode confinement, which requires increasing the cross-section of the microring (H, W) to mitigate the surface scattering loss. However, this will be constrained by the desire to decrease the mode volume, that is, to increase the mode field strength at the atomic trap location $|\mathcal{E}(\rho_{\mathrm{t}}, z_{\mathrm{t}})|^2$. Moreover, the radius of the microring cannot be reduced indefinitely because of the increased bending loss and the surface scattering loss at the sidewall (the guided mode shifts toward the outer edge of the microring, as shown in Fig. S1). An optimized geometry balances the requirement for proper mode confinement and small mode volume to achieve high Q/V_{m}.

REFERENCES

1. M. Oxborrow, "Traceable 2-d finite-element simulation of the whispering-gallery modes of axisymmetric electromagnetic resonators," IEEE Transactions on Microw. Theory Tech. **55**, 1209–1218 (2007).
2. M. I. Cheema and A. G. Kirk, "Implementation of the perfectly matched layer to determine the quality factor of axisymmetric resonators in comsol," in *COMSOL conference*, (2010).
3. M. Borselli, T. J. Johnson, and O. Painter, "Beyond the rayleigh scattering limit in high-q silicon microdisks: theory and experiment," Opt. Express **13**, 1515–1530 (2005).
4. X. Ji, F. A. S. Barbosa, S. P. Roberts, A. Dutt, J. Cardenas, Y. Okawachi, A. Bryant, A. L. Gaeta, and M. Lipson, "Ultra-low-loss on-chip resonators with sub-milliwatt parametric oscillation threshold," Optica **4**, 619–624 (2017).
5. M. H. P. Pfeiffer, J. Liu, A. S. Raja, T. Morais, B. Ghadiani, and T. J. Kippenberg, "Ultra-smooth silicon nitride waveguides based on the damascene reflow process: fabrication and loss origins," Optica **5**, 884–892 (2018).
6. K. Srinivasan and O. Painter, "Mode coupling and cavity–quantum-dot interactions in a fiber-coupled microdisk cavity," Phys. Rev. A **75**, 023814 (2007).
7. D. Ding, A. Goban, K. Choi, and H. Kimble, "Corrections to our results for optical nanofiber traps in cesium," arXiv preprint arXiv:1212.4941 (2012).
8. F. Le Kien, P. Schneeweiss, and A. Rauschenbeutel, "Dynamical polarizability of atoms in arbitrary light fields: general theory and application to cesium," The Eur. Phys. J. D **67**, 92 (2013).
9. F. Payne and J. Lacey, "A theoretical analysis of scattering loss from planar optical waveguides," Opt. Quantum Electron. **26**, 977–986 (1994).
10. C. G. Poulton, C. Koos, M. Fujii, A. Pfrang, T. Schimmel, J. Leuthold, and W. Freude, "Radiation modes and roughness loss in high index-contrast waveguides," IEEE J. selected topics quantum electronics **12**, 1306–1321 (2006).
11. M. Kuznetsov, "Radiation loss in dielectric waveguide y-branch structures," J. Light. Technol. **3**, 674–677 (1985).